



Combination of porous covalent triazine frameworks with spinel for highly improved photothermal catalytic oxidation of toluene

Xunxun Li, Yaru Wang, Jiaqin He, Jun Xiao, Wanjun Xu, Dongyun Chen^{*}, Najun Li, Qingfeng Xu, Hua Li, Jianmei Lu^{*}

College of Chemistry, Chemical Engineering and Materials Science, Collaborative Innovation Center of Suzhou Nano Science and Technology, Soochow University, Suzhou 215123, China

ARTICLE INFO

Keywords:

Toluene
Adsorption
Oxygen vacancies
Photothermal catalytic

ABSTRACT

The synergistic effect of adsorption and photothermal can be used to develop new efficient pollutant treatment technologies. Here, porous covalent triazine frameworks modified CuO@CoMn₂O₄ catalyst (PCTF-CCM) was constructed and applied to the full spectrum driven photothermal degradation of toluene. Toluene conversion and CO₂ yield over PCTF-CCM under simulated solar irradiation (optical power density=350 mW/cm²) could be reached 100% and 98% with 40 min. Oxygen vacancies play an important role in thermal and photothermal catalysis by enhancing the adsorption of pollutant gases and the mobility of oxygen. The porous covalent triazine frameworks enriched the concentration of pollutants on the surface of catalyst and significantly improved the water resistant capability, leading to the performance of photothermal catalytic oxidation of toluene highly improved. The designed system extends the range and service life of catalyst in practical applications and provides a new idea for the design of adsorption-photothermal catalyst.

1. Introduction

The continuous emission of volatile organic compounds (VOCs) not only causes serious environmental problems but also poses a great threat to people's health [1–3]. Therefore, effective, economical and environmentally friendly removal of volatile organic pollutants is an important research topic. At present, the technologies used to remove VOCs mainly include adsorption, thermal catalysis, photocatalysis, and photothermal catalysis [4–8]. Traditional thermal catalysts consume large amounts of energy and are prone to poisoning by water vapor, which reduces the activity of the catalyst [9–11]. Photocatalytic oxidation of toluene can reduce the energy consumption of catalytic reaction, but this degradation method cannot completely remove toluene [12–16]. Single traditional technology is difficult to meet the requirements of efficient VOC removal, so two or more technologies can be developed to improve the removal efficiency of volatile organic pollutants.

In order to meet the requirements of low energy consumption and high catalytic performance, it is necessary to develop stable adsorption photothermal catalysts. The combined technology of adsorption and catalysis can rapidly enrich pollutants on the surface of the catalyst, thereby improving the catalytic reaction rate [17–19]. Photothermal

catalysis combines the advantages of thermal catalysis and photocatalysis to remove VOCs. This method can effectively avoid additional energy supply and avoid catalyst being poisoned by water vapor [20–22]. Combined with the advantages of adsorption and photothermal catalyst technology, it can achieve rapid and high degradation rate VOC removal [23–25]. Therefore, it is necessary to develop adsorption-photothermal catalysts.

Transition metal oxides (TMOs) are considered promising alternatives for noble metal-based catalysts used in VOC combustion owing to their low cost and high oxygen storage capacity [26–30]. Manganese oxide (MnO_x) has the advantages of good activity, stability, wide light absorption range, and low cost, and thus it is a promising catalyst for the photothermal degradation of VOCs [31–34]. For example, Ye et al. synthesized layered porous α -MnO₂/Mn₃O₄ hybrids by topological transformation and found that α -MnO₂/Mn₃O₄ is stable and can promote the photothermal removal of toluene [35]. Cobalt has also been studied extensively owing to its capacity to host abundant reactive oxygen species [36–38]. Co_{3–x}O_{4–y} catalysts with cobalt defects and oxygen vacancies have been reported to show remarkable photothermal catalytic performance for toluene oxidation [39]. However, the performance of catalysts based on cobalt and manganese is poorer than that of

^{*} Corresponding authors.

E-mail addresses: dychen@suda.edu.cn (D. Chen), lujm@suda.edu.cn (J. Lu).

catalysts based on precious metals. Therefore, it is of great significance to design high-performance catalysts based on TMOs through structural design and surface modification.

Oxygen vacancies enhance thermal catalytic gas phase reactions by promoting lattice oxygen migration [40–42]. Oxygen vacancy is the most active site in photocatalysis, which can promote the formation of superoxide radical ($\cdot\text{O}_2^-$), thus strengthening the adsorption of pollutants [27]. Generally, oxygen vacancies can be introduced into catalysts by doping, reduction, and vacuum deoxidation. Feng et al. reported that copper oxide is an ideal material for photothermal conversion [43]. Therefore, using copper oxide as a nano heater to construct cobalt-manganese based photothermal catalysts with oxygen vacancies is worthy of further study.

Zeolite, carbon materials and porous organic polymers are commonly used in the adsorption of VOCs [44–46]. Porous organic polymers have high specific surface area, controllable pore size and superior stability. It is considered as a potential adsorption material. Recently, Shang et al. [47] reported the application of a super cross-linked conjugated polymer in VOC adsorption. It was shown that multiple hydrogen bonds are formed between PCTF-CCM and the VOCs.

In this work, spinel oxide coated with porous covalent triazine frameworks were synthesized for highly improved photothermal catalytic oxidation of toluene, as shown in Scheme 1. The catalysts of $\text{CuO@CoMn}_2\text{O}_4$ was synthesized by hydrothermal method. Subsequently, the porous covalent triazine frameworks were constructed on the surface of the photothermal catalyst by amino modification, polymerization and foucault reaction, and finally catalyst with adsorption and photothermal catalysis was obtained (PCTF-CCM). In addition, oxygen vacancies were constructed on the surface of $\text{CuO@CoMn}_2\text{O}_4$ by reduction treatment. By modifying the porous covalent triazine frameworks, the adsorption of toluene was promoted, thus accelerating catalytic reaction rate. The high temperature energy consumption required by traditional catalytic reaction is reduced through adsorption photothermal degradation technology. This work provides a reference way to achieve low energy consumption and efficient removal of pollutants in the air.

2. Experimental section

2.1. Materials

All materials used in this research are described in the

Supplementary Materials section.

2.2. Sample preparation

2.2.1. Synthesis of CoMn_2O_4 and Mn_2O_3

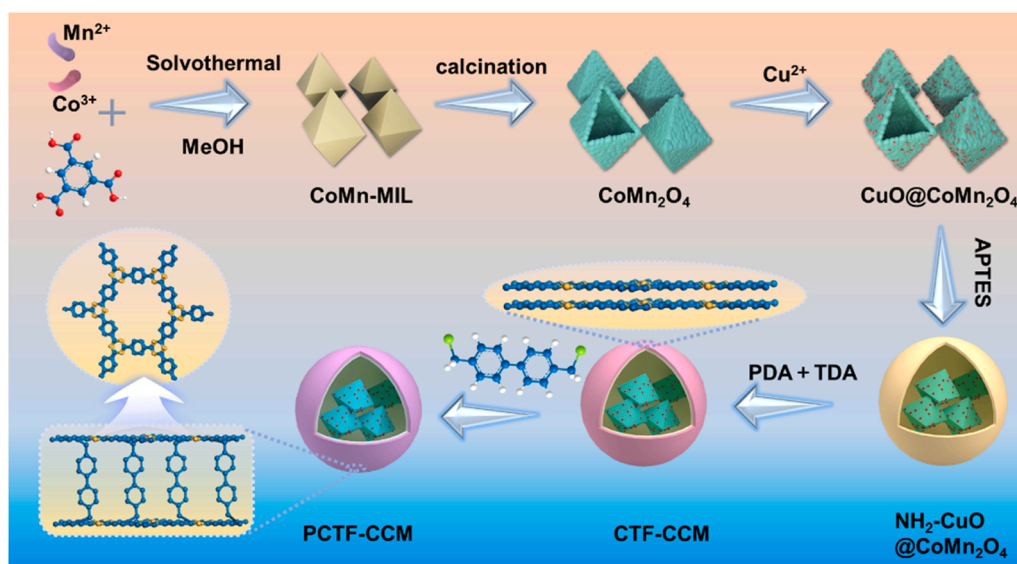
CoMn_2O_4 and Mn_2O_3 were synthesized according to the modified synthesis method reported in the previous literature [48].

2.2.2. Synthesis of $\text{CuO@CoMn}_2\text{O}_4$ with oxygen vacancy

The oxygen vacancy was constructed by NaBH_4 reduction. First, 0.3 g of the prepared CoMn_2O_4 powder was dispersed into 100 mL $\text{Cu}(\text{NO}_3)_2$ ultrapure water and stirred continuously in a boiling water bath for 1 h. Then 5 mL (1 mol/L) NaOH and 0.1 mol/L NaBH_4 fresh mixed solution were added and stirred continuously for 20 min. After the reaction, the powder is filtered, washed and dried. Finally, the obtained powder is calcined in air at 250 °C for 2 h. By adjusting the amount of $\text{Cu}(\text{NO}_3)_2$, different proportions of $\text{CuO@CoMn}_2\text{O}_4$ were obtained. According to the results of ICP calibration, it was named 5 wt% $\text{CuO@CoMn}_2\text{O}_4$, 10 wt% $\text{CuO@CoMn}_2\text{O}_4$, 15 wt% $\text{CuO@CoMn}_2\text{O}_4$.

2.2.3. Synthesis of PCTF-CCM

First, the catalyst 10 wt% $\text{CuO@CoMn}_2\text{O}_4$ is modified with amino group, and the detailed steps are shown in the support information. The preparation of PCTF-CCM and CTF-CCM were according to the previous study [47,49]. First, 150 mg $\text{NH}_2\text{-CuO@CoMn}_2\text{O}_4$ was dissolved in 100 mL DMSO and uniformly dispersed by ultrasound. Then 0.016 g of p-benzaldehyde was added and stirred at 60 °C for 12 h. Then, 0.056 g of terephthalamidine dihydrochloride and 0.240 g of cesium carbonate are added to the above reaction system, and they react at 60 °C and 80 °C for 12 h respectively. Finally, 0.051 g of terephthalaldehyde, 0.179 g of terephthalamidine dihydrochloride and 0.480 g of cesium carbonate are added to the above reaction system, and they react at 100 and 120 °C for 24 h respectively. The product was washed twice with deionized water and DMF, and the last time was washed with deionized water. The product is named CTF-CCM. A mixture containing 120 mg CTF-CCM, 125 mg 4,4-Bis(chloromethyl)biphenyl and 160 mg FeCl_3 were added in 30 mL of DCE and ultrasound for 1 h. Then the reactant is stirred continuously for 24 h under the protection of nitrogen at 90 °C. The product is obtained by washing with H_2O and DMF, named PCTF-CCM.



Scheme 1. Schematic illustration of the synthesis of PCTF-CCM.

2.3. Characterization

X-ray powder diffraction (XRD) patterns were recorded on a Bruker D8 Advance X-ray diffractometer with Cu K α radiation ($\lambda = 1.5406 \text{ \AA}$) in the 2θ range between 5° and 80° . Scanning electron microscopy (SEM) was carried out with a Regulus 8230 field-emission scanning electron microscope. Transmission electron microscopy (TEM) and high-resolution TEM (HRTEM) were carried out with Tecnai G2 F20. X-ray photoelectron spectroscopy (XPS) measurements were performed on EXCALAB 250 XI spectrometer. Elemental analysis of samples was detected by ICPOES. The Brunauer-Emmett-Teller (BET) surface area and pore distribution were determined by means of a Belsorp II mini machine (BEL Japan). H $_2$ temperature programmed reduction (H $_2$ -TPR) and Toluene-TPD were performed on MicrotracBEL. The JES-X320 system is used for electron paramagnetic resonance (EPR) measurement. In situ diffuse reflectance infrared Fourier transform spectroscopy (in situ DRIFTS) was used to characterize the conversion pathway of toluene.

2.4. Performance test of thermal catalysis and photothermal catalysis for toluene

The thermal and photothermal properties of toluene were evaluated in a fixed-bed reactor and a quartz reaction tube on the PLR-PTSRIII Photothermal catalytic reaction system. In the thermocatalytic process, the reaction temperature was controlled by a temperature-controlled electric furnace. In the photothermal catalytic reaction process, 300 W Xe lamp was used in the side of the reactor to provide light exposure to the adiabatic reaction window. UV-visible-infrared light ($\lambda = 300\text{--}2500 \text{ nm}$) was used to simulate sunlight. The temperature of the catalyst surface was measured by thermocouple. The equilibrium concentration of toluene gas was 500 ppm (in equilibrium with air) and the flow rate was 30 mL/min (WHSV = 36,000 mL/(h·g)). Toluene and carbon dioxide concentrations were determined by gas chromatography (FID detector). The conversion rate, reaction rate and reaction activation energy of toluene were calculated by the following equation:

$$\text{Toluene Conversion}(\text{X}_{\text{toluene}}, \%) = \frac{\text{Toluene}_{\text{in}} - \text{Toluene}_{\text{out}}}{\text{Toluene}_{\text{in}}} \times 100\%$$

Water resistance was tested using the PLR-PTSRIII Photo-Thermal

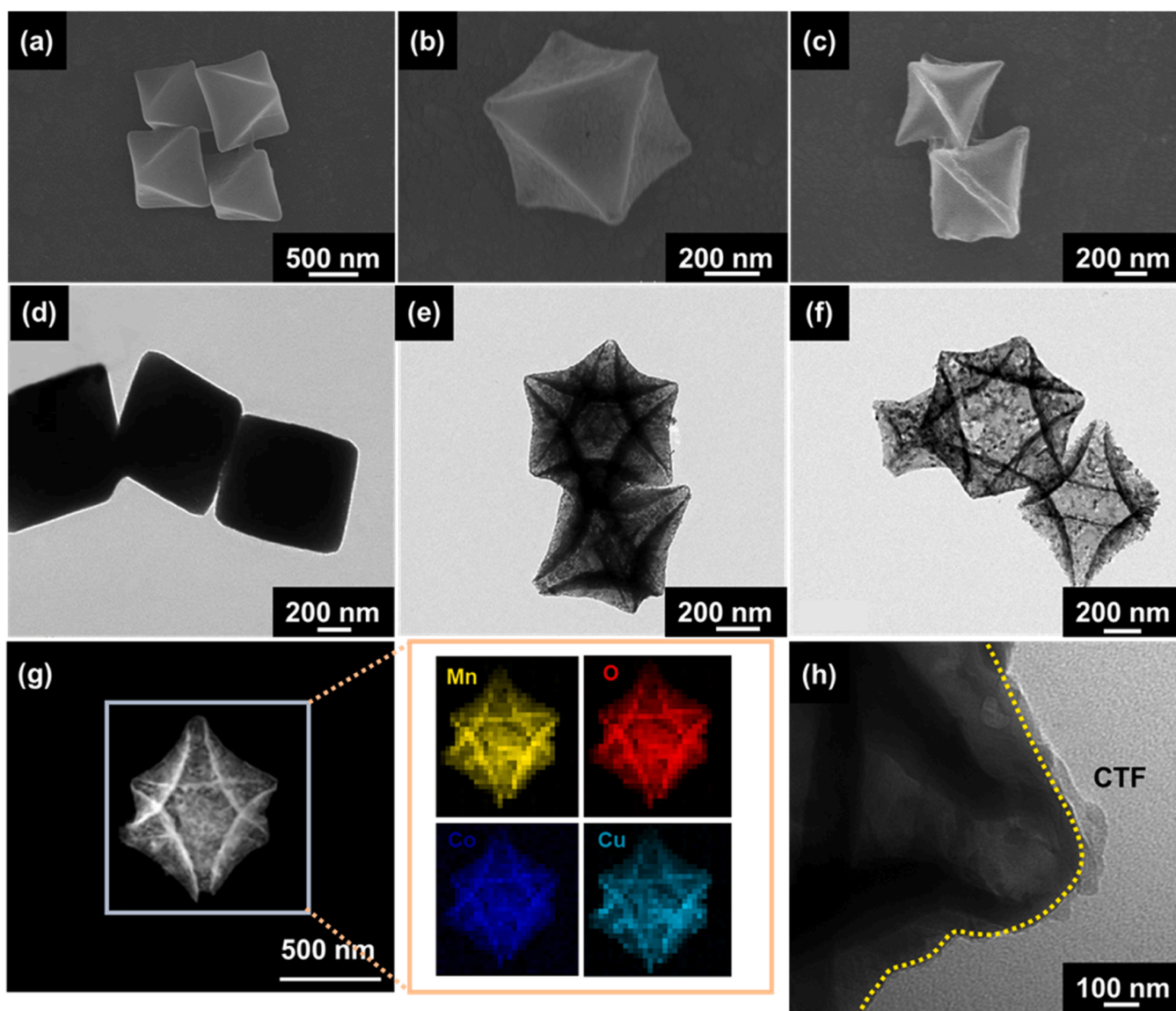


Fig. 1. SEM images of (a) CoMn-MIL, (b) CoMn $_2$ O $_4$ and (c) 10 wt% CuO@CoMn $_2$ O $_4$. TEM images of (d) CoMn-MIL, (e) CoMn $_2$ O $_4$ and (f) 10 wt% CuO@CoMn $_2$ O $_4$. (h) TEM images of CTF-CCM.

Catalytic Reaction System (Beijing Perfectlight), where liquid water was added to the vaporizing device and the desired volume of water vapor was obtained by controlling the flow rate.

3. Results and discussion

3.1. Morphology and structure characterization

The morphology of the sample was investigated using field emission scanning electron microscopy (SEM) and transmission electron microscopy (TEM). The SEM and TEM images (Fig. 1a, d) showed that the obtained CoMn-MIL had a uniform smooth surface and an octahedral shape. The average particle sizes of Mn-MIL and CoMn-MIL were 1.09 μm and 600 nm, respectively. Therefore, introducing cobalt significantly decreased the particle size of Mn-MIL (Fig. S1). As shown in Fig. 1h, Mn-MIL and CoMn-MIL had the same crystal structure, consistent with previously reported data. Moreover, the XRD diffraction peak of CoMn-MIL had a significantly lower intensity than that of Mn-MIL (Fig. S2), confirming that introducing cobalt limited crystal growth. Calcination roughened the surface and reduced the particle size of CoMn-MIL. CuO nanoparticles were deposited on the surface of CoMn₂O₄, and oxygen vacancies were generated. Introducing CuO nanoparticles led to the appearance of voids on the catalyst surface corresponding to defects on the catalyst surface produced after the NaBH₄ treatment, which was supported by the SEM and TEM images of CuO@CoMn₂O₄ (Fig. 1c, f). Elemental mapping revealed that Cu, O, Mn, and Co were uniformly distributed in CuO@CoMn₂O₄. From Fig. 1h, it can be clearly observed that CTF was modified on the surface of the catalyst. It proved that the adsorption photothermal catalyst was successfully prepared.

The crystal structure and phase composition of Mn₂O₃, CoMn₂O₄, and CuO@CoMn₂O₄ were analyzed by XRD (Fig. 2a). XRD analysis showed that thermal decomposition of CoMn-MIL produced CoMn₂O₄ (JCPDS#01-1126), while thermal decomposition of Mn-MIL produced Mn₂O₃ (JCPDS#41-1442). Owing to the low content of loaded copper

oxide, the intensity of the CuO diffraction peak was low, although EDX mapping and XPS data indicated the existence of copper. The N₂ adsorption-desorption isotherms and pore size distribution of the samples are shown in Fig. 2a-b, and details of the pore structure are shown in Table S1. As shown in Fig. 2b, the adsorption curve was inconsistent with the desorption curve, and there was an obvious hysteresis loop, indicating that the obtained isotherm was a type IV isotherm. Fig. 2c shows the pore size distribution of the catalyst. Details of the surface area and pore size distribution of the catalyst are listed in Table S1. The surface area of PCTF-CCM was 2.3 times higher than that of the unmodified catalyst. In addition, the average aperture of PCTF-CCM is extended to 14 nm. Such a structure can expose more adsorption sites and facilitate the transport of gas molecules. The FT-IR spectra of the synthesized materials are shown in Fig. 2d. The successful formation of triazine structures in CTF-CCM and PCTF-CCM were confirmed by the C=N stretching bands (1510 and 811 cm^{-1}) and C-N stretching vibration band (1366 cm^{-1}) in the FT-IR spectra. Vibration bands observed at 2971 cm^{-1} corresponded to the -CH₂- stretching vibrations only appeared in the spectra of PCTF-CCM, proved the successful introduction of molecular expansion agent.

3.2. Surface structure analysis

To investigate the composition and charge distribution of surface oxygen species, X-ray photoelectron spectroscopy (XPS) was carried out. As shown in Fig. 3c, the two peaks at 529.7 and 531.3 eV were attributed to surface lattice oxygen (O_L) and surface adsorbed oxygen (O_A), respectively. The proportion of adsorbed oxygen reflects the concentration of oxygen vacancies in the catalyst. As shown in Table S1, the O_A/O_L ratios of Mn₂O₃, CoMn₂O₄, 5 wt% CuO@CoMn₂O₄, 10 wt% CuO@CoMn₂O₄, and 15 wt% CuO@CoMn₂O₄ were 0.33, 0.35, 0.46, 0.60, and 0.50, respectively. This confirmed that using the sodium borohydride reduction method to load CuO also efficiently introduced oxygen vacancies into the catalyst. Fig. 3d shows the Co 2p XPS spectra of the catalysts. The peaks at 780.16 and 795.24 eV were assigned to

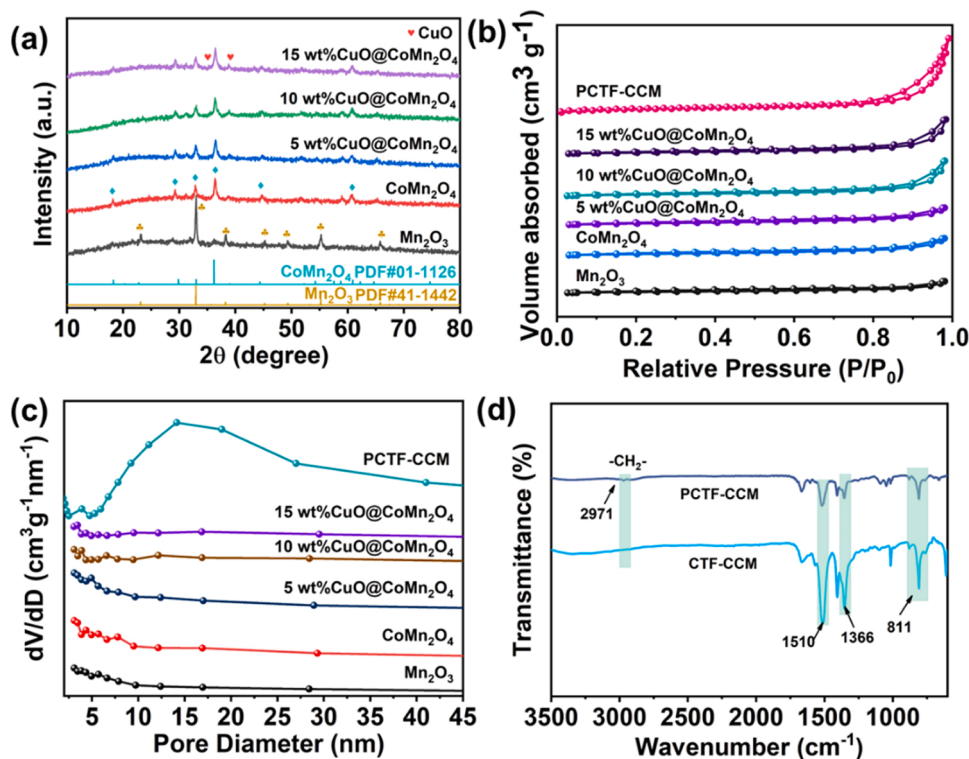


Fig. 2. (a) XRD patterns, (b) N₂ adsorption-desorption isotherms, and (c) pore size distributions of Mn₂O₃, CoMn₂O₄, CuO@CoMn₂O₄ and PCTF-CCM. (d) FT-IR spectra of the PCTF-CCM and CTF-CCM.

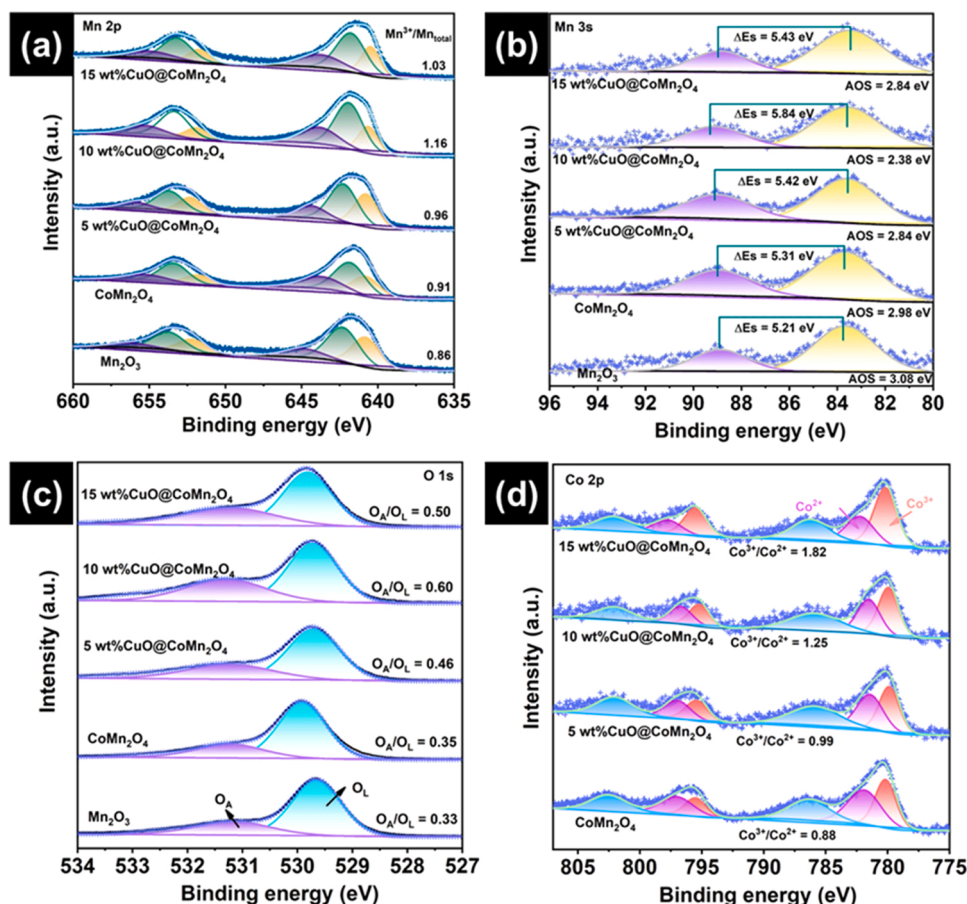


Fig. 3. (a) Mn 2p, (b) Mn 3s, and (c) O 1s XPS spectra of Mn_2O_3 , CoMn_2O_4 , and $\text{CuO@CoMn}_2\text{O}_4$. (d) Co 2p XPS spectra of CoMn_2O_4 and $\text{CuO@CoMn}_2\text{O}_4$.

Co^{3+} , while the other two peaks at 781.5 and 797.1 eV were determined to derive from Co^{2+} . The Mn 2p XPS spectra (Fig. 3a) contained peaks centered at 641.79 and 652.87 eV corresponding to Mn 2p 3/2 and Mn 2p 1/2, respectively. Each peak was deconvoluted into three peaks using the binding energy of Mn^{2+} (640.68 eV), Mn^{3+} (642.0 eV), and Mn^{4+} (644.5 eV). It is worth noting that the Mn^{3+} -O bond is longer and weaker than the Mn^{4+} -O bond, and thus a high proportion of Mn^{3+} indicates that the catalyst surface contains weak Mn-O bonds, which facilitates the release of oxygen for participation in catalytic oxidation. In addition, Mn^{3+} promotes the dissociation and release of other oxygen species in the catalyst. In general, the Mn^{3+} concentration is used to reflect the oxygen vacancy content in the catalyst. This is because the catalyst produces oxygen vacancies to maintain the electrostatic balance as the Mn^{3+} concentration in the catalyst increases. As shown in Table S1,

$\text{Mn}^{3+}/\text{Mn}_{\text{total}}$ in the different catalysts, calculated using XPS spectral data, increased in the order of 10 wt% $\text{CuO@CoMn}_2\text{O}_4$ > 15 wt% $\text{CuO@CoMn}_2\text{O}_4$ > 5 wt% $\text{CuO@CoMn}_2\text{O}_4$ > CoMn_2O_4 > Mn_2O_3 . We can infer that the concentration of oxygen vacancies in the sample is compounded by the reactions restoring electrostatic balance. In addition, the average oxidation state of the catalyst can be calculated using the formula of average oxidation state (AOS): $\text{AOS} = 8.956 - 1.126 \Delta\text{Es}$, where ΔEs refers to the binding energy between the two peaks of Mn 3s (Fig. 3b). The calculated AOS of 10 wt% $\text{CuO@CoMn}_2\text{O}_4$ was the lowest, which further confirmed that the concentration of oxygen vacancies in 10 wt% $\text{CuO@CoMn}_2\text{O}_4$ was high. In addition, the XPS spectrum (Fig. S1) of the catalyst confirmed the existence of each element in the catalyst.

According to the literature, reducibility is an important factor to

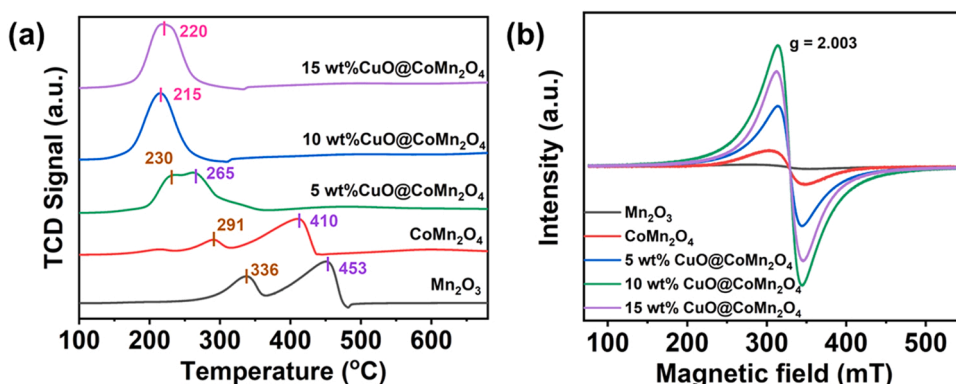


Fig. 4. (a) H₂-TPR curves and (b) EPR spectra of Mn_2O_3 , CoMn_2O_4 , and $\text{CuO@CoMn}_2\text{O}_4$.

evaluate the performance of catalyst. As shown in Fig. 4a, each catalyst has a reduction peak below 500 °C. With the addition of copper oxide, the reduction peak of the catalyst shifted to a low temperature, indicating that its reducibility was increased. The H₂ consumption of catalyst was further obtained through the reduction peak of H₂-TPR, and it was concluded that the consumption of catalyst 10 wt% CuO@CoMn₂O₄ was the largest. Therefore, it can be predicted that the catalyst has excellent catalytic activity. Oxygen vacancies on the surface or subsurface of catalysts can be detected using electron paramagnetic resonance (EPR) spectroscopy. Therefore, oxygen vacancies in the catalyst was further investigated with EPR. The signal at $g = 2.003$ attributed to paramagnetic oxygen vacancies corresponds to the unpaired electrons in the oxygen vacancy of the metal oxide (Fig. 4b). In addition, the intensity of the EPR signal reflects the concentration of oxygen vacancies. Generally, the stronger the signal, the higher the oxygen vacancy concentration. We can see from Fig. 4b that 10 wt% CuO@CoMn₂O₄ had the highest oxygen vacancy concentration, which also validated the XPS observation.

3.3. Adsorption performance for toluene

In order to investigate the adsorption behavior of the prepared adsorption-catalyst on toluene, Toluene-TPD experiment was carried out. The peak strength and desorption temperature of toluene reasonably reflect the adsorption capacity of the catalyst. In Fig. 5a, compared with the photothermal catalyst alone, CTF-CCM increased toluene adsorption capacity by 3.17 times. The adsorption of toluene by PCTF-CCM was 4.84 times higher than that of the basic photothermal catalyst. This result proves that the introduction of expansion agent provides more adsorption sites. It has been reported in the literature that the covalent triazine frameworks interacts with toluene to form multiple hydrogen bonds and π - π accumulation, which enhances the adsorption of toluene. In addition, the saturated adsorption capacity of the catalyst 10 wt% CuO@CoMn₂O₄ was evaluated by dynamic adsorption experiments. As can be seen from Fig. 5b, the catalyst showed the shortest breakthrough time and the lowest adsorption capacity, and the modification of covalent triazine significantly increased the adsorption capacity of the material. Fig. 5c lists the adsorption capacity of toluene by different materials as follows: 10 wt% CuO@CoMn₂O₄ < CTF-CCM < PCTF-CCM.

3.4. Thermal and photothermal catalytic oxidation of toluene

The effect of oxygen vacancy concentration on the activity of the catalysts during the thermal catalytic oxidation of toluene was evaluated. The mineralization of toluene in the presence of each catalyst was studied at different temperatures. As shown in Fig. 6a, the Mn₂O₃ catalyst, produced by the pyrolysis of Mn-MIL, had catalytic activity, but the temperature required for complete transformation was 240 °C. The

catalytic performance of CoMn₂O₄, produced by the pyrolysis of CoMn-MIL, was greater than that of Mn₂O₃. This suggests that catalytic performance increases as the concentration of oxygen vacancies in the catalyst increases, with occurs with the introduction of cobalt, as demonstrated by the XPS and ESR analyses. Additionally, the performance of catalysts with different loaded copper oxide contents increased in the order of 5 wt% CuO@CoMn₂O₄ < 15 wt% CuO@CoMn₂O₄ < 10 wt% CuO@CoMn₂O₄. The apparent activation energy (E_a) of the catalysts was calculated using the Arrhenius equation (Fig. 6b). The activation energy of 10 wt% CuO@CoMn₂O₄ was the lowest, consistent with the performance results. Moreover, the reaction rate of thermal catalysis over 10 wt% CuO@CoMn₂O₄ was 11.94 $\mu\text{mol g}^{-1}\text{s}^{-1}$, which was 1.24 times that over Mn₂O₃ and 1.19 times that over CoMn₂O₄ (Fig. 6c). We also tested the long-term stability of the catalysts. Specifically, toluene conversion over Mn₂O₃, CoMn₂O₄, and 10 wt% CuO@CoMn₂O₄ was stable at 37%, 52%, 75% over a period of 16 h at 180 °C (Fig. 6d). According to the above results, 10 wt% CuO@CoMn₂O₄ showed the best thermal catalytic performance.

Based on the data of the performance of the thermal catalytic oxidation of toluene, we modified a layer of covalent triazine frameworks on the surface of the best catalyst 10 wt% CuO@CoMn₂O₄, and then carried out a series of investigations of the photothermal catalytic performance. When the catalyst is illuminated by light, the non-radiative relaxation of photogenerated electrons can convert the solar energy into heat energy, so we measured the temperature change of the catalyst surface by thermocouple. As shown in Fig. 7a, within 10 min the temperature of the catalyst surface becomes stable. The surface temperature of catalyst 10 wt% CuO@CoMn₂O₄ is the highest, which can reach 210 °C. At the same time, we also found that the surface temperature of the catalyst did not change significantly after the surface modification of covalent triazine, indicating that the porous structure of covalent triazine did not weaken the photothermal effect of the catalyst. In Fig. 7b, it is found that CTF-CCM and PCTF-CCM have excellent catalytic properties in the photothermal conversion of toluene. The results show that the adsorption- photothermal co-catalytic technology can significantly improve the catalytic performance of the catalyst. Among them, PCTF-CCM can achieve 100% conversion and 98% yield of CO₂ within 40 min. In addition, it can be seen from Fig. 7c that the concentration of carbon dioxide is higher in the initial stage, which is due to the adsorption of toluene on the catalyst surface. As shown in Fig. 7d, the apparent activation energy (E_a) of catalysts under irradiation was calculated through the Arrhenius equation. The E_a value of the PCTF-CCM catalyst is the lowest, which is 36.5 kJ mol⁻¹. In addition, the apparent activation energy (E_a) under irradiation and dark conditions was displayed in Fig. S3. It can be observed that the activation energy under light irradiation is lower than that under thermal condition. Therefore, the photothermal effect promotes the activity of the catalyst.

The comparison of photocatalytic performance of catalysts for

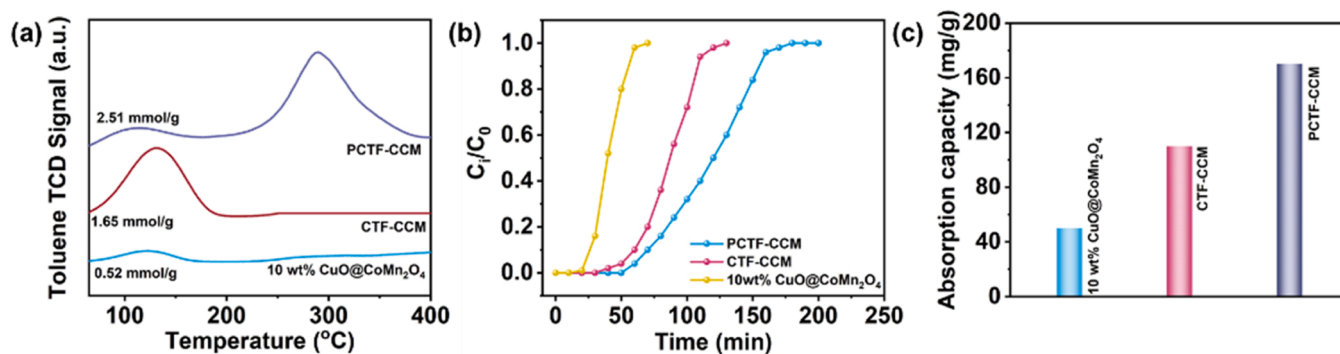


Fig. 5. (a) Toluene-TPD patterns of the synthesized samples. (b) Dynamic adsorption breakthrough curves of the synthesized samples. (c) Adsorption capacity of the synthesized samples.

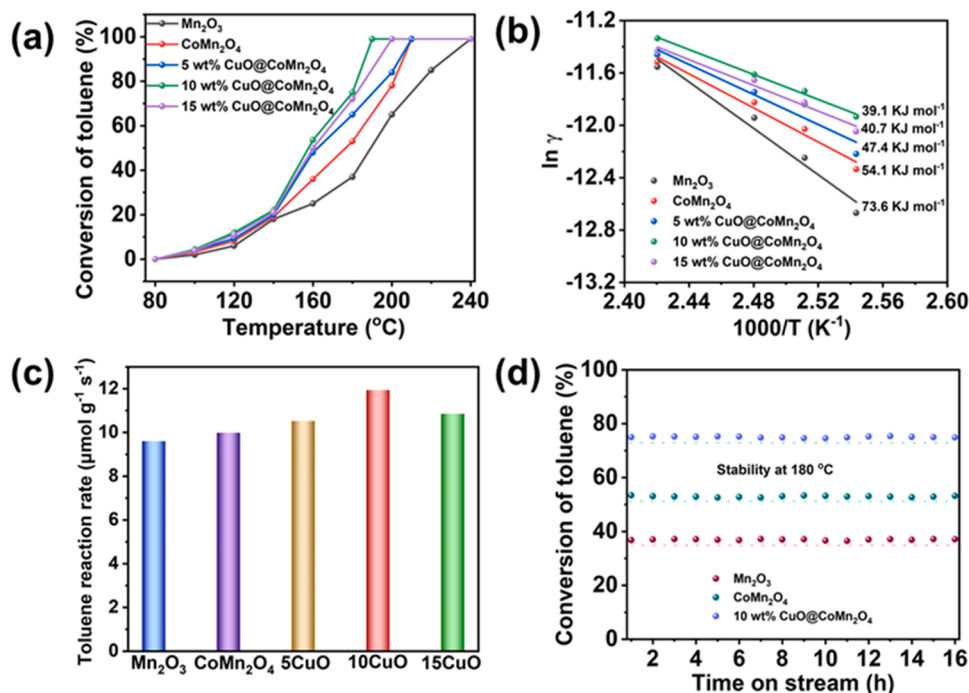


Fig. 6. (a) Plots of toluene conversion versus temperature over various catalysts. (b) Arrhenius plots for catalytic toluene oxidation over various catalysts. (d) Reaction rate of thermal catalysis over various catalysts. (e) Stability of Mn_2O_3 , CoMn_2O_4 , and 10 wt% $\text{CuO@CoMn}_2\text{O}_4$ at 180 °C.

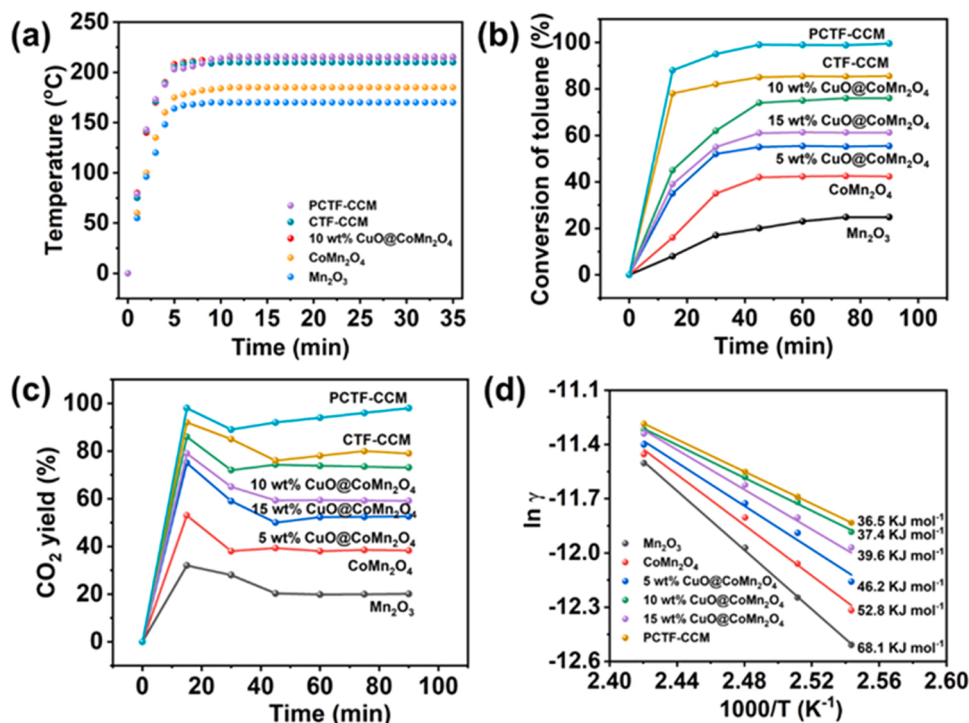


Fig. 7. (a) Surface temperature of catalyst under simulated solar irradiation (optical power density = 350 mW/cm²) by thermocouple. (b) Photothermal catalytic properties of toluene. Reaction conditions: 500 ppm of toluene balanced with 21% O_2/N_2 , total flow rate of 30 mL/min, light intensity 350 mW/cm². (c) CO_2 selectivity of each catalyst in photothermal catalytic oxidation. (d) Activation energy of photothermal catalytic oxidation of toluene on different catalysts.

toluene is shown in Table 1. It indicates that the catalyst (PCTF-CCM) has better catalytic activity (100% Toluene conversion) under low light intensity (350 mW/cm²).

We examined the reactive oxygen species using EPR. Reactive oxygen species were detected using the DPMO free radical trapping agent. As shown in Fig. 8, 10 wt% $\text{CuO@CoMn}_2\text{O}_4$ was used to detect signals

arising from $\bullet\text{O}_2$ and $\bullet\text{OH}$. Under dark conditions, no signal peaks were detected. However, after illumination for 2 min, $\bullet\text{O}_2$ and $\bullet\text{OH}$ peaks were observed, indicating that reactive oxygen species were produced under light conditions.

Table 1
Summary of published articles on photothermal catalytic oxidation of toluene.

Catalyst	Space velocity (mL g ⁻¹ h ⁻¹)	Light	C _{Toluene} (ppm)	Toluene conversion	Ref.
0.39Pt ₁ /CuO-CeO ₂	20,000	Full spectrum 200 mW/cm ²	200	100%	[43]
3%Na-Co ₃ O ₄	-	Full spectrum 425 mW/cm ²	400	89.8%	[26]
Cu _{1.5} Mn _{1.5} O ₄	30,000	Full spectrum 350 mW/cm ²	200	98%	[50]
CoTi	30,000	Full spectrum 900 mW/cm ²	200	90%	[51]
ZMO-H	36,000	Full spectrum 500 mW/cm ²	200	93%	[52]
PCTF-CCM	36,000	Full spectrum 350 mW/cm ²	500	100%	This work

3.5. Mechanism of thermal and photothermal catalytic oxidation of toluene

To investigate the mechanism of the thermal and photothermal catalytic oxidation of toluene, in situ diffuse-reflectance infrared Fourier-transform spectroscopy (DRIFTS) was used to track the changes in intermediate species. The conversion of toluene by oxidation over PCTF-CCM catalyst is shown in Fig. 9. The adsorption band at 2310 cm⁻¹ was assigned to CO₂, and the broad band at 3231 cm⁻¹ was assigned to H₂O. The characteristic peak of benzyl alcohol species (PhCH₂OH) was located at 1027 cm⁻¹. The peak centered at 1423 cm⁻¹ was assigned to benzaldehyde species (PhCHO). In addition, the bands at 1202, 1384, and 1495 cm⁻¹ were assigned to benzoic acid species (PhCOOH), and the band at 1296 cm⁻¹ was assigned to maleic anhydride. These species are important intermediates in the degradation of toluene. The conversion processes at different temperatures were investigated by collecting in-situ infrared spectra of the time-dependent thermal and photothermal catalytic degradation of toluene. In situ DRIFTS analysis showed that toluene was quickly adsorbed on the catalyst surface and reacted with oxygen species to form benzyl alcohol, benzaldehyde, and benzoate species, which completely oxidized to CO₂ and H₂O.

The adsorption photothermal catalytic degradation mechanism of toluene is shown in Scheme 2. In general, toluene can be completely converted into water and carbon dioxide without additional heating. Covalent triazine frameworks plays an important role in adsorption. Low-concentration toluene is enriched on the catalyst surface. When the catalyst is continuously exposed to light, the strong photothermal capacity drives the temperature of the catalyst to rise to the equilibrium

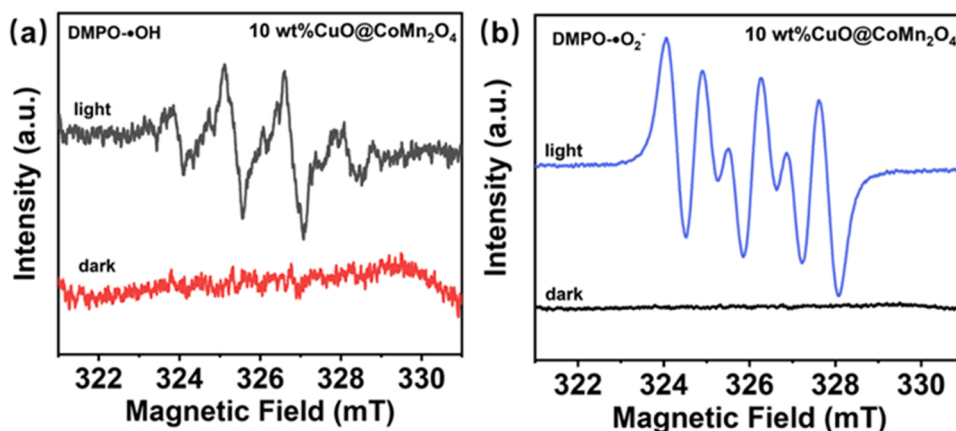


Fig. 8. DMPO spin-trapping EPR spectra for (a) •OH and (b) •O₂.

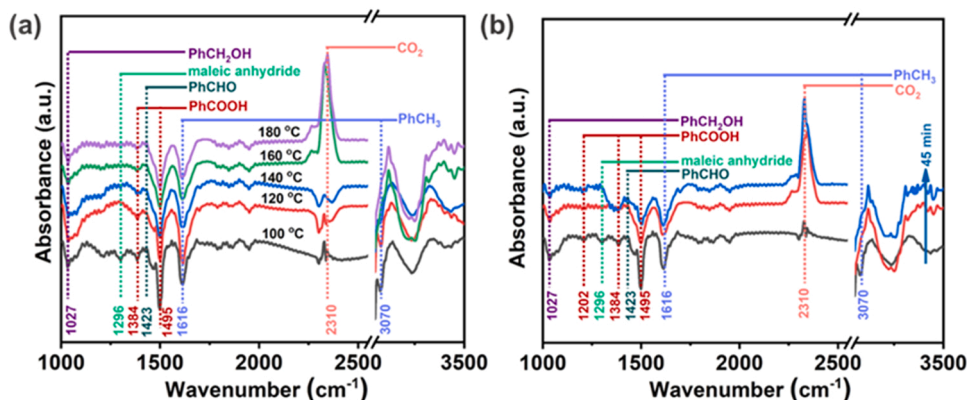
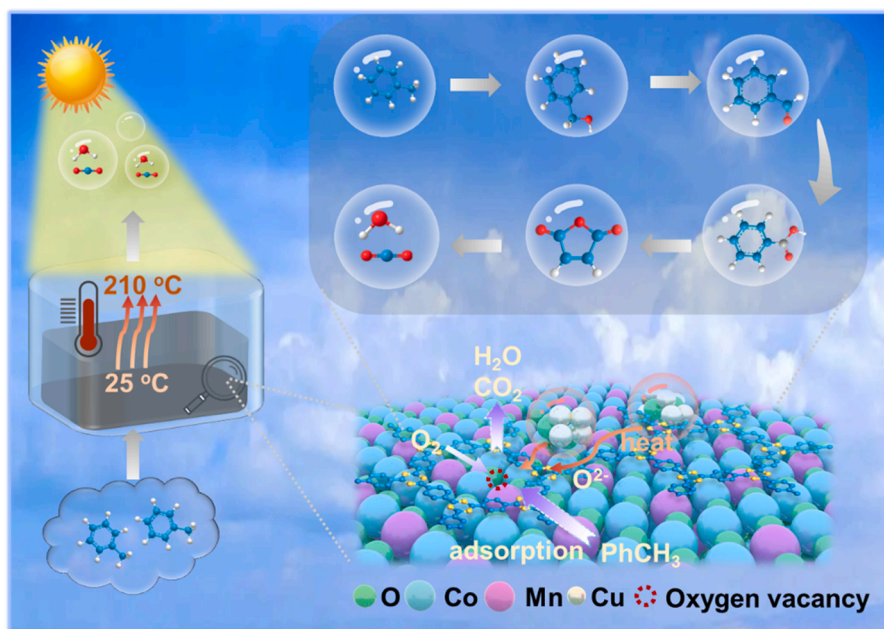


Fig. 9. In situ DRIFTS spectra of the (a) thermal and (b) photothermal catalytic oxidation of toluene over PCTF-CCM.



Scheme 2. Schematic diagram of the mechanism of photothermal catalytic oxidation of toluene.

temperature and induces the active oxygen to oxidize toluene. In addition, the superoxide radicals produced under light irradiation promote the mineralization of toluene. Rich oxygen vacancies can promote the adsorption of gaseous oxygen and facilitate the migration of lattice oxygen, so that the catalyst can generate active oxygen faster. According to the in-situ infrared data, toluene is degraded through the following conversion process: toluene \rightarrow benzyl alcohol \rightarrow benzaldehyde \rightarrow benzoates \rightarrow CO_2 and H_2O .

In practical applications, the catalyst activity is often reduced due to the presence of water vapor. Therefore, we tested the water resistance of the catalyst under the conditions of thermal and photothermal catalysis. Fig. 10 shows the water resistance of the catalyst under traditional heating conditions. Under dry conditions, toluene conversion by catalytic oxidation was more than 90%. After water vapor was introduced with toluene, the performance of the catalyst decreased. When water vapor was removed, the performance of the catalyst gradually recovered, but it did not return to the original performance. This shows that under the condition of traditional thermal catalysis, water vapor competes with oxygen for catalytic active sites on the catalyst surface, which inhibits the activity of the catalyst. The effect of water vapor on the

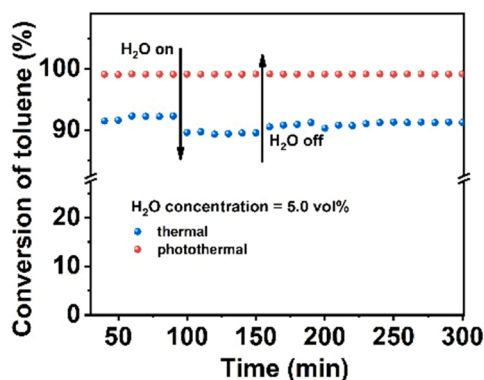


Fig. 10. Catalytic oxidation performance of the catalyst PCTF-CCM for toluene under humid environmental. Reaction conditions: 500 ppm of toluene (5.0 vol % H_2O) balanced with 21% O_2/N_2 , total flow rate of 30 mL/min (WHSV = 36,000 mL/(h·g)).

photothermal catalytic oxidation of toluene over PCTF-CCM is shown in Fig. 10, revealing that a small amount of water vapor does not poison the catalyst. Therefore, using PCTF-CCM for the photothermal catalytic oxidation of toluene can reduce energy consumption as well as prevent catalyst poisoning.

4. Conclusion

In summary, an adsorption catalytic material composed of porous covalent triazine frameworks and spinel was successfully prepared for the catalytic oxidation of toluene. The as-synthesized PCTF-CCM catalyst exhibited excellent toluene deep oxidation performance, achieving complete conversion of toluene under simulated solar irradiation ($350 \text{ mW}/\text{cm}^2$) without additional heating. The porous covalent triazine frameworks were engineered on the surface of the catalyst with the best performance, which promoted the adsorption of toluene on the catalyst, thus accelerating the catalytic reaction rate. The superior catalytic activity can be attributed to the high concentration of oxygen vacancy, low-temperature reducibility and photothermal conversion capability. Most importantly, the designed catalyst maintained a stable working state in the presence of water vapor and exhibited excellent water resistance. In addition, the reaction pathway of toluene catalytic oxidation was studied by in situ DRIFTS and it was concluded that the photothermal reaction pathway also followed the Langmuir-Hinshelwood (L-H) reaction mechanism. This paper provides a new perspective for the adsorption photothermal oxidation of toluene.

CRediT authorship contribution statement

Xunxun Li: Conceptualization, Methodology, Writing – original draft. **Yaru Wang:** Software, Investigation. **Jiaqin He:** Software, Methodology. **Jun Xiao & Wanjun Xu:** Methodology, Investigation. **Najun Li:** Data curation, Formal analysis. **Qingfeng Xu:** Visualization, Writing – review & editing. **Hua Li:** Software, Validation. **Jianmei Lu & Dongyun Chen:** Supervision, Writing – review & editing.

Declaration of Competing Interest

The authors declare that they have no known competing financial interests or personal relationships that could have appeared to influence

the work reported in this paper.

Data availability

Data will be made available on request.

Acknowledgements

We gratefully acknowledge the financial support provided by the National Key R&D Program of China (2020YFC1808401), National Natural Science Foundation of China (22078213, 21938006, 51973148, 21776190), Cutting-edge Technology Basic Research Project of Jiangsu (BK20202012) and the project supported by the Priority Academic Program Development of Jiangsu Higher Education Institutions (PAPD).

Appendix A. Supporting information

Supplementary data associated with this article can be found in the online version at [doi:10.1016/j.apcatb.2023.122690](https://doi.org/10.1016/j.apcatb.2023.122690).

References

- [1] K. Zhang, H. Ding, W. Pan, X. Mu, K. Qiu, J. Ma, Y. Zhao, J. Song, Z. Zhang, Research progress of a composite metal oxide catalyst for VOC degradation, *Environ. Sci. Technol.* 56 (2022) 9220–9236.
- [2] K. Vohra, E.A. Marais, W.J. Bloss, J. Schwartz, L.J. Mickley, M. Van Damme, L. Clarisse, P.-F. Coheur, Rapid rise in premature mortality due to anthropogenic air pollution in fast-growing tropical cities from 2005 to 2018, *Sci. Adv.*, 8 eabm4435.
- [3] S. Gu, A. Guenther, C. Faiola, Effects of anthropogenic and biogenic volatile organic compounds on Los Angeles air quality, *Environ. Sci. Technol.* 55 (2021) 12191–12201.
- [4] B. Liu, J. Ji, B. Zhang, W. Huang, Y. Gan, D.Y.C. Leung, H. Huang, Catalytic ozonation of VOCs at low temperature: a comprehensive review, *J. Hazard. Mater.* 422 (2022), 126847.
- [5] C. Yang, G. Miao, Y. Pi, Q. Xia, J. Wu, Z. Li, J. Xiao, Abatement of various types of VOCs by adsorption/catalytic oxidation: a review, *Chem. Eng. J.* 370 (2019) 1128–1153.
- [6] R. Liu, H. Wu, J. Shi, X. Xu, D. Zhao, Y.H. Ng, M. Zhang, S. Liu, H. Ding, Recent progress on catalysts for catalytic oxidation of volatile organic compounds: a review, *Catal. Sci. Technol.* (2022).
- [7] Q. Yu, J. Li, W. Liu, Y. Wang, W. Chu, X. Zhang, L. Xu, X. Zhu, X. Li, Rational design of a novel Silica-Based material with abundant open micropores for efficient VOC removal, *Chem. Eng. J.* 454 (2023), 140077.
- [8] M. Yan, Y. Rong, F. Wu, Z. You, D. Wang, X. Yang, Z. Hao, J. Li, Z. Zhang, Microporous graphitized carbon fiber as hydrophobic adsorbent that removes volatile organic compounds from air, *Chem. Eng. J.* 452 (2023), 139184.
- [9] X. Wu, R. Han, Q. Liu, Y. Su, S. Lu, L. Yang, C. Song, N. Ji, D. Ma, X. Lu, A review of confined-structure catalysts in the catalytic oxidation of VOCs: synthesis, characterization, and applications, *Catal. Sci. Technol.* 11 (2021) 5374–5387.
- [10] Y. Guo, M. Wen, G. Li, T. An, Recent advances in VOC elimination by catalytic oxidation technology onto various nanoparticles catalysts: a critical review, *Appl. Catal. B Environ.* 281 (2021), 119447.
- [11] M. Xiao, D. Han, X. Yang, N. Tsona Tchinda, L. Du, Y. Guo, Y. Wei, X. Yu, M. Ge, Ni-doping-induced oxygen vacancy in Pt-CeO₂ catalyst for toluene oxidation: enhanced catalytic activity, water-resistance, and SO₂-tolerance, *Appl. Catal. B Environ.* 323 (2023), 122173.
- [12] L. Yang, J. Guo, T. Yang, C. Guo, S. Zhang, S. Luo, W. Dai, B. Li, X. Luo, Y. Li, Self-assembly Cu₂O nanowire arrays on Cu mesh: a solid-state, highly-efficient, and stable photocatalyst for toluene degradation under sunlight, *J. Hazard. Mater.* 402 (2021), 123741.
- [13] L. Chen, P. Chen, H. Wang, W. Cui, J. Sheng, J. Li, Y. Zhang, Y. Zhou, F. Dong, Surface lattice oxygen activation on Sr₂Sb₂O₇ enhances the photocatalytic mineralization of toluene: from reactant activation, intermediate conversion to product desorption, *ACS Appl. Mater. Interfaces* 13 (2021) 5153–5164.
- [14] J. Zhang, Y. Hu, J. Qin, Z. Yang, M. Fu, TiO₂-UiO-66-NH₂ nanocomposites as efficient photocatalysts for the oxidation of VOCs, *Chem. Eng. J.* 385 (2020), 123814.
- [15] L. Chen, K. Li, Y. Yang, T. Xue, H. Wang, B. Lei, J. Sheng, F. Dong, Y. Sun, Amorphous SnO₂ decorated ZnSn(OH)₆ promotes interfacial hydroxyl polarization for deep photocatalytic toluene mineralization, *J. Hazard. Mater.* 444 (2023), 130436.
- [16] K. Zhang, H. Chen, Y. Liu, J. Deng, L. Jing, A. Rastegarpanah, W. Pei, Z. Han, H. Dai, Two-dimensional Bi₂W₂Mo_{1-x}O₆ solid solution nanosheets for enhanced photocatalytic toluene oxidation to benzaldehyde, *Appl. Catal. B Environ.* 315 (2022), 121545.
- [17] J. Wang, X. Gao, Y. Wang, S. Wang, Z. Xie, B. Yang, Z. Zhang, Z. Yang, L. Kang, W. Yao, Multifunctional core-double-shell C@MnO@TiO₂ catalysts with enhanced full-light conversion for the highly efficient photothermal oxidation of toluene, *Appl. Catal. B Environ.* 317 (2022), 121789.
- [18] Y. Du, G. Xiao, Z. Guo, B. Lin, M. Fu, D. Ye, Y. Hu, A high-performance and stable Cu/Beta for adsorption-catalytic oxidation in-situ destruction of low concentration toluene, *Sci. Total Environ.* 833 (2022), 155288.
- [19] S. Sonar, J.-M. Giraudon, J.-F. Lamonier, R. Morent, N. De Geyter, A. Löfberg, Toluene removal by a sequential adsorption-thermal catalytic process on Ag/Hopcalite, *ChemCatChem* (2022), e202200926.
- [20] J. Kong, C. Jiang, Z. Rui, S. Liu, F. Xian, W. Ji, H. Ji, Photothermocatalytic synergistic oxidation: an effective way to overcome the negative water effect on supported noble metal catalysts for VOCs oxidation, *Chem. Eng. J.* 397 (2020), 125485.
- [21] Y. Li, S. Wu, J. Wu, Q. Hu, C. Zhou, Photothermocatalysis for efficient abatement of CO and VOCs, *J. Mater. Chem. A* 8 (2020) 8171–8194.
- [22] C. Liang, C. Li, Y. Zhu, X. Du, Y. Zeng, Y. Zhou, J. Zhao, S. Li, X. Liu, Q. Yu, Y. Zhai, Light-driven photothermal catalysis for degradation of toluene on CuO/TiO₂ Composite: dominating photocatalysis and auxiliary thermalcatalysis, *Appl. Surf. Sci.* 601 (2022), 154144.
- [23] J. Huang, X. Ye, W. Li, A. Shi, X. Chu, Z. Cao, C. Yao, X. Li, Infrared-to-visible upconversion enhanced photothermal catalytic degradation of toluene over Yb³⁺, Er³⁺: CeO₂/attapulgite nanocomposite: effect of rare earth doping, *J. Ind. Eng. Chem.* 116 (2022) 504–514.
- [24] M. Zhang, S. Cai, J. Li, E.A. Elimian, J. Chen, H. Jia, Ternary multifunctional catalysts of polymeric carbon nitride coupled with Pt-embedded transition metal oxide to enhance light-driven photothermal catalytic degradation of VOCs, *J. Hazard. Mater.* 412 (2021), 125266.
- [25] J.-J. Li, S.-C. Cai, X. Chen, D.-X. Yan, J. Chen, H.-P. Jia, Engineering rGO nanosheets-adsorption layer supported Pt nanoparticles to enhance photo-thermal catalytic activity under light irradiation, *J. Mater. Chem. A* 7 (2019) 11985–11995.
- [26] W. Dai, M. Zou, C. Zhao, J. Zhang, L. Wang, X. Wang, L. Yang, L. Zhou, J. Zou, X. Luo, S. Luo, G. Jing, Monoatomic oxygen fueled by oxygen vacancies governs the photothermocatalytic deep oxidation of toluene on Na-doped Co₃O₄, *Appl. Catal. B Environ.* 317 (2022), 121769.
- [27] X. Wei, K. Li, X. Zhang, Q. Tong, J. Ji, Y. Cai, B. Gao, W. Zou, L. Dong, CeO₂ nanosheets with anion-induced oxygen vacancies for promoting photocatalytic toluene mineralization: toluene adsorption and reactive oxygen species, *Appl. Catal. B Environ.* 317 (2022), 121694.
- [28] J. Gao, Z. Si, Y. Xu, L. Liu, Y. Zhang, X. Wu, R. Ran, D. Weng, Pd-Ag@CeO₂ catalyst of core-shell structure for low temperature oxidation of toluene under visible light irradiation, *J. Phys. Chem. C* 123 (2019) 1761–1769.
- [29] Y. Luo, Z. Chi, J. Zhang, B. Tian, Photothermocatalytic system designed by facet-heterojunction to enhance the synergistic effect of toluene oxidation, *ChemCatChem* 14 (2022), e202101958.
- [30] X. Chen, S. Cai, E. Yu, J. Li, J. Chen, H. Jia, Photothermocatalytic performance of ACo₂O₄ type spinel with light-enhanced mobilizable active oxygen species for toluene oxidation, *Appl. Surf. Sci.* 484 (2019) 479–488.
- [31] D. Fu, L. Duan, C. Jiang, T. Zhang, W. Chen, Nanostructured manganese oxides exhibit facet-dependent oxidation capabilities, *Environ. Sci. Nano* 7 (2020) 3840–3848.
- [32] R. Yang, Z. Guo, L. Cai, R. Zhu, Y. Fan, Y. Zhang, P. Han, W. Zhang, X. Zhu, Q. Zhao, Z. Zhu, C.K. Chan, Z. Zeng, Investigation into the phase-activity relationship of MnO₂ nanomaterials toward ozone-assisted catalytic oxidation of toluene, *Small* 17 (2021), 2103052.
- [33] J. Su, Q. Ke, H. Xu, Hierarchically MnO₂/SiO₂ nanocomposites with high solar light-driven photo-thermo catalysis activity for efficient toluene removal, *Appl. Surf. Sci.* 608 (2023), 155177.
- [34] X. Zhang, Z. Ma, Z. Song, H. Zhao, W. Liu, M. Zhao, J. Zhao, Role of cryptomelane in surface-adsorbed oxygen and Mn chemical valence in MnO_x during the catalytic oxidation of toluene, *J. Phys. Chem. C* 123 (2019) 17255–17264.
- [35] P. Wu, S. Dai, G. Chen, S. Zhao, Z. Xu, M. Fu, P. Chen, Q. Chen, X. Jin, Y. Qiu, S. Yang, D. Ye, Interfacial effects in hierarchically porous α -MnO₂/Mn₃O₄ heterostructures promote photocatalytic oxidation activity, *Appl. Catal. B Environ.* 268 (2020), 118418.
- [36] W. Zhang, J. Díez-Ramírez, P. Anguita, C. Descorme, J.L. Valverde, A. Giroir-Fendler, Nanocrystalline Co₃O₄ catalysts for toluene and propane oxidation: effect of the precipitation agent, *Appl. Catal. B Environ.* 273 (2020), 118894.
- [37] Q. Ren, S. Mo, J. Fan, Z. Feng, M. Zhang, P. Chen, J. Gao, M. Fu, L. Chen, J. Wu, D. Ye, Enhancing catalytic toluene oxidation over MnO₂@Co₃O₄ by constructing a coupled interface, *Chin. J. Catal.* 41 (2020) 1873–1883.
- [38] A. Rokicińska, M. Drozdek, B. Dudek, B. Gil, P. Michorczyk, D. Brouri, S. Dzwigaj, P. Kuśtrowski, Cobalt-containing BEA zeolite for catalytic combustion of toluene, *Appl. Catal. B Environ.* 212 (2017) 59–67.
- [39] Y. Li, T. Chen, S. Zhao, P. Wu, Y. Chong, A. Li, Y. Zhao, G. Chen, X. Jin, Y. Qiu, D. Ye, Engineering cobalt oxide with coexisting cobalt defects and oxygen vacancies for enhanced catalytic oxidation of toluene, *ACS Catal.* 12 (2022) 4906–4917.
- [40] Z. Su, W. Yang, C. Wang, S. Xiong, X. Cao, Y. Peng, W. Si, Y. Weng, M. Xue, J. Li, Roles of oxygen vacancies in the bulk and surface of CeO₂ for toluene catalytic combustion, *Environ. Sci. Technol.* 54 (2020) 12684–12692.
- [41] W. Hong, Y. Liu, T. Zhu, H. Wang, Y. Sun, F. Shen, X. Li, Promoting the catalytic ozonation of toluene by introducing SO₄²⁻ into the α -MnO₂/ZSM-5 catalyst to tune both oxygen vacancies and acid sites, *Environ. Sci. Technol.* (2022).
- [42] J. Zeng, H. Xie, Z. Liu, X. Liu, G. Zhou, Y. Jiang, Oxygen vacancy induced MnO₂ catalysts for efficient toluene catalytic oxidation, *Catal. Sci. Technol.* 11 (2021) 6708–6723.
- [43] Y. Feng, L. Dai, Z. Wang, Y. Peng, E. Duan, Y. Liu, L. Jing, X. Wang, A. Rastegarpanah, H. Dai, J. Deng, Photothermal synergistic effect of Pt₁/CuO-

- CeO₂ single-atom catalysts significantly improving toluene removal, *Environ. Sci. Technol.* 56 (2022) 8722–8732.
- [44] X. Meng, L. Meng, Y. Gong, Z. Li, G. Mo, J. Zhang, Modifying Y zeolite with chloropropyl for improving Cu load on Y zeolite as a super Cu/Y catalyst for toluene oxidation, *RSC Adv.* 11 (2021) 37528–37539.
- [45] J. Qin, J. Wang, J. Yang, Y. Hu, M. Fu, D. Ye, Metal organic framework derivative-TiO₂ composite as efficient and durable photocatalyst for the degradation of toluene, *Appl. Catal. B Environ.* 267 (2020), 118667.
- [46] L. Lan, Y. Huang, Y. Dan, L. Jiang, Conjugated porous polymers for gaseous toluene adsorption in humid atmosphere, *React. Funct. Polym.* 159 (2021), 104804.
- [47] Q. Shang, Y. Cheng, Z. Gong, Y. Yan, B. Han, G. Liao, D. Wang, Constructing novel hyper-crosslinked conjugated polymers through molecular expansion for enhanced gas adsorption performance, *J. Hazard. Mater.* 426 (2022), 127850.
- [48] Y. Zeng, Y. Wang, Q. Jin, Z. Pei, D. Luan, X. Zhang, X.W. Lou, Rationally designed Mn₂O₃-ZnMn₂O₄ hollow heterostructures from metal-organic frameworks for stable Zn-ion storage, *Angew. Chem. Int. Ed.* 60 (2021) 25793–25798.
- [49] N. Wang, G. Cheng, L. Guo, B. Tan, S. Jin, Hollow covalent triazine frameworks with variable shell thickness and morphology, *Adv. Funct. Mater.* 29 (2019), 1904781.
- [50] Q. Cheng, Z. Wang, X. Wang, J. Li, Y. Li, G. Zhang, A novel Cu_{1.5}Mn_{1.5}O₄ photothermal catalyst with boosted surface lattice oxygen activation for efficiently photothermal mineralization of toluene, *Nano Res.* (2022).
- [51] Y. Yang, S. Zhao, F. Bi, J. Chen, Y. Wang, L. Cui, J. Xu, X. Zhang, Highly efficient photothermal catalysis of toluene over Co₃O₄/TiO₂ p-n heterojunction: the crucial roles of interface defects and band structure, *Appl. Catal. B Environ.* 315 (2022), 121550.
- [52] Q. Cheng, Y. Li, Z. Wang, X. Wang, G. Zhang, Boosting full-spectrum light driven surface lattice oxygen activation of ZnMn₂O₄ by facet engineering for highly efficient photothermal mineralization of toluene, *Appl. Catal. B Environ.* 324 (2023), 122274.